

A Study of the Fundamental Relationships between Deformation-Induced Surface Roughness and Strain Localization in AA5754

M.R. STOUTD, J.B. HUBBARD, M.A. IADICOLA, and S.W. BANOVIC

Three-dimensional, matrix-based statistical analysis methods were developed and integrated with high-resolution topographical imaging, to assess how microstructural changes influence the evolution of plastic deformation and strain localization in a commercial AA5754-O aluminum sheet in three in-plane strain modes. Analysis of the raw surface data revealed that the general composition of the surface roughness was highly sensitive to strain mode and strain level. The microstructural conditions that promote strain localization were assessed by extending a profile-based surface roughness parameter (Rt) to matrix form. Both analyses revealed that different strain modes produce characteristic dissimilarities in the deformation at the grain level. The localization data can be well characterized with a two-parameter Weibull distribution, suggesting that strain localization is a stochastic process that can be modeled reliably with Weibull statistics. This study clearly demonstrates that an accurate and straightforward probabilistic expression that captures the microstructural subtleties produced by plastic deformation can be developed from rigorous analyses of raw topographic data. Because variations in surface morphology profoundly influence the reliability of the numerical models used to predict strain localization, incorporating expressions of this type could greatly enhance the accuracy of these models.

DOI: 10.1007/s11661-009-9881-6

© The Minerals, Metals & Materials Society and ASM International 2009

I. INTRODUCTION

THE introduction of new alloys into the automobile body is an expensive and time-consuming process. For this reason, numerical predictions of the formability of metal sheet have become integral components in the automotive design process, generating a strong demand for accurate and reliable predictions of mechanical behavior under a wide range of deformation conditions. The inability to reliably model the evolution of the surface inhomogeneities produced during sheet metal forming creates a significant obstacle that impedes the widespread incorporation of these alloys. One of the most common approaches to assessing the formability, and thus the suitability, of an alloy for a particular application is the forming limit diagram. It is well known that macroscopic deformation in a typical metal stamping occurs through a combination of strain modes, or paths (*e.g.*, biaxial, uniaxial, and plane strain). Considering that a combination of strain modes will likely promote failure at an overall strain that is lower than would be expected if the deformation occurred in a single strain mode, it is essential that the relative influence of each component of the macroscopic strain

combination be properly identified and accurately assessed. Such a characterization is a complicated process requiring numerous high-resolution measurements of the deformation under each strain mode.^[1] Consequently, the limiting strains in a typical stamping are most often estimated *via* numerical simulations specifically designed to predict the onset of macroscopic, or gross, strain localization. These complex simulations are usually based on phenomenological constitutive relations that assume a homogeneous response to an imposed macroscopic strain at the microstructural level until the onset of localization.^[2] Accordingly, significant deviations from the homogeneous response are then considered to indicate the onset of a critical localization event (*i.e.*, a direct precursor to failure such as the formation of cracks or splits, necks, *etc.*).^[3]

Even though models based on this approach tend to correctly indicate the general trends, they often fail to consistently predict the precise strains at which localization occurs.^[4] The addition of revised plasticity and kinematic hardening models and the results from studies of the influence of various material parameters (such as grain size and grain orientation effects, surface roughening effects, and other damage mechanisms) on strain localization have enhanced the reliability of the numerical models.^[5-12] Despite the significant improvements that have been made to these models, inconsistencies still exist between the mechanical behavior that is predicted and the behavior that is observed experimentally. One possible source for these discrepancies is that the models used to predict the mechanical behavior are

M.R. STOUTD, M.A. IADICOLA and S.W. BANOVIC, Materials Research Engineers, and J.B. HUBBARD, Research Associate, are with the NIST Center for Metal Forming, Materials Science and Engineering Laboratory, National Institute of Standards and Technology, Gaithersburg, MD 20899. Contact e-mail: stoutd@nist.gov
Manuscript submitted October 22, 2008.

fundamentally deterministic and they simply cannot account for all of the variability that is possible in every microstructural component involved in the plastic deformation process of a polycrystalline material. In many cases, the complexity of the microstructural effects is often greatly simplified, to reduce the required computational time.

Clearly, plastic deformation in a polycrystalline alloy is extremely complex and the evolved surface is the result of many factors.^[13] Most mechanical deformation models incorporate microstructural and surface roughness effects to some extent, as a means of estimating the local deformation conditions that promote strain localization. Unfortunately, the fidelity of the roughness data used in these models is questionable, given that these data are routinely based on the erroneous assumption of a linear relationship between the surface roughness and the plastic strain.^[11,14,15] The literature also indicates that the strain mode has little or no influence on the measurable surface roughness, if the grain size is constant.^[16]

The results of a recent evaluation of deformation-induced surface roughness with plastic strain plainly demonstrated that the linear relationship between the surface root-mean-squared (RMS) roughness (Sq) and the plastic strain reported in the literature is a statistical artifact resulting from inadequate sampling.^[17] That is, such a simple expression relating strain and deformation-induced surface roughness does not accurately reflect the true deformation behavior of the free surface of a polycrystalline material. The findings of this study^[17] also reveal that the linear relationship between surface roughness and strain is a consequence of the methods used to acquire and analyze the roughness data. The assessments of the roughening behavior in the literature are largely derived from sets of linear profiles; they express the surface roughness as the simple average of a single scalar roughness parameter that describes the dispersion of heights within the profiles about the mean (e.g., Ra , the arithmetic average roughness, or Rq , the RMS average roughness). The character of the entire surface at a particular strain level (i.e., \bar{X}_{Rq}) is then represented by this “average” roughness parameter. When it is calculated from the mean of individual profiles, the “roughness” becomes highly sensitive to the sampling conditions and to the influence of the natural ordering (i.e., sequences or correlations) present in the profile data.^[18] In addition, this approach generates an ensemble of Rq distributions in which each sample in the ensemble has its own mean and variance. The total number of possible ensembles and the magnitude of the statistical uncertainty associated with each ensemble then become a function of the sampling parameters. (That is, $\bar{X}_{Rq} \neq Sq$, under these sampling conditions.)

If one considers a deformed surface as a composite consisting of the topographical characteristics produced by each mechanism that was active during the deformation process, it then becomes reasonable to assert that integrating high-resolution topographical measurements and analysis methods that minimize the statistical uncertainty will improve our understanding of how changes in microstructure influence the evolution of plastic

deformation and, ultimately, critical strain localization. This then raises the following question: Can carefully designed surface topography measurements be used to reliably predict critical strain localization? Such a prediction is predicated on accurate assessments, or maps, of the morphological conditions that promote strain localization. These maps must be derived from multiple sets of surface roughness data scrupulously acquired from a range of deformation conditions that capture the scope of the microstructural variations and minimize the statistical uncertainty in the roughness data.

This article presents a study of strain localization behavior in three in-plane strain modes for a commercial AA5754-O aluminum sheet, as determined from detailed topographic analyses. The motivation for this research is the concept of mapping microstructural changes that occur as a function of plastic deformation, such as has been shown by Frost and Ashby,^[19] Greenwood,^[20] and Mohamed and Langdon.^[21] The measurement and sampling protocols used in this study are based on high-resolution topographical imaging techniques and rigorous matrix-based, three-dimensional statistical analysis methods. This article is part of a larger effort designed to understand and predict the factors that determine the multiaxial flow surface for automotive alloys. This more general study includes detailed characterizations of the relative changes that occur in the crystallographic texture with strain level in the same three in-plane strain modes,^[22] the parametric analyses of the relative influences of strain with the strain mode,^[1] and the evolution of multiaxial flow surfaces.^[23] The relationships among the individual elements of this general study will be presented in future studies.

II. EXPERIMENTAL

A. Material

The aluminum alloy selected for this study, AA5754-O, was developed primarily for automotive applications. Like most alloys in the 5xxx series, AA5754 is substitutionally strengthened and demonstrates good overall formability. It also exhibits discontinuous yielding of the Portevin-Le Châtelier (PLC) type (i.e., PLC banding) that has been characterized in the literature.^[23–26] As reported by The Aluminum Association (Arlington, VA), AA5754 typically contains 2.8 pct mass fraction Mg for solid-solution strengthening and approximately 0.5 pct mass fraction Mn for grain refinement and stability.^[27] Metallographic examination revealed that the grain structure was relatively equiaxed in the rolling plane and slightly elongated along the rolling direction (RD) of the sheet. This is indicative of the recrystallized microstructure normally associated with the O-temper. The mean grain size for this alloy was approximately $40 \pm 20 \mu\text{m}$.^[22]

B. Generation of Surface Roughness

A set of $30 \times 30 \text{ cm}$ ($12 \times 12 \text{ in.}$) blanks was sheared from 1-mm-thick sheet stock for testing. When the

tensile axis of rolled sheet specimens lies in the transverse orientation to the RD, the evolved surface roughness tends to be slightly more severe than when the tensile axis is parallel to the RD.^[17] Therefore, the scope of this study focused on samples deformed in the transverse direction.

Industry customarily uses aluminum sheet stock in the as-received condition, O-temper, with a specified maximum acceptable initial surface roughness that varies with the particular application. While it is important to represent actual forming conditions, the mill scale present on most commercial aluminum alloys completely obscures the fine surface features that evolve during the initial stages of the deformation process, thereby making high-resolution measurements of these characteristics extremely difficult. As such, the specimens in this evaluation were polished to reveal the surface character at low strains and to produce more consistent surface roughness measurements. Preparation consisted of mechanically polishing one side to a 6- μm diamond finish using a metallographic polishing technique that was based on standard metallurgical procedure.^[28]

After polishing, the blanks were deformed in three in-plane strain modes defined in terms of the in-plane principal true strain ratio ($\rho = \frac{\epsilon_2}{\epsilon_1}$). The first strain ratio was $\rho = 1$ (hereafter referred to as equibiaxial); the second strain ratio was $\rho = -0.5$ (hereafter referred to as uniaxial); and the third strain ratio was $\rho = 0$ (hereafter referred to as plane strain). The uniaxial samples were machined to an ASTM E08-91 standard-sheet-type tensile specimen geometry. The specimens were then strained according to standard test methods^[29] at a constant displacement rate that produced a strain rate of $6 \times 10^{-4} \text{ s}^{-1}$ to nominal true strain values of 5, 10, and 15 pct. Both the equibiaxial and plane strain deformations were imposed using an augmentation^[30] of the Marciniak flat-bottom ram test.^[3] Samples were strained in equibiaxial tension using a typical strain rate of $5 \times 10^{-4} \text{ s}^{-1}$ to nominally 5, 10, 15, and 20 pct true first-principal strain (ϵ_1). A third set of samples was strained to similar true strain levels in the plane strain condition. Additionally, one sample was taken to failure in each strain mode. Note that, for purposes of this study, “failure” refers to the maximum uniform strain outside of the region in which gross localization occurred. Therefore, the surface roughness data acquired at this condition establish the maximum uniform surface roughness obtainable for the AA5754-O alloy in each strain mode. Coupons were cut from the center of each deformed specimen for topographic analysis.

C. Surface Roughness Measurements

The surface topography was quantified for each strain level in each strain mode with scanning laser confocal microscopy (SLCM). Each measurement in this evaluation consisted of five well-spaced SLCM images taken from the specimen surface. The imaging conditions were the same for each evaluation; they consisted of an objective lens (10 times) and a nominal total z-scan depth of approximately 40 μm . These parameters

generated sets of 640×512 -pixel intensity images with 12-bit resolution. The spacing between sampling points in the (x, y) plane was fixed by the objective lens at 1.56 μm ; the spacing between the focal planes within each image was approximately 100 nm. This produces images with nominal physical dimensions (x, y, z) of $1000 \times 800 \times 40 \mu\text{m}$. The SLCM stores each topographic image data as a raw tagged image file format (TIFF) depth map that contains the full set of imaging parameters and binary pixel values. A computer code was developed that uses the format standards within a TIFF image to convert the bit values into a simple numerical matrix of surface heights. The resulting matrix was then trimmed to a square 512×512 -pixel ($800 \times 800\text{-}\mu\text{m}$) 262,144-element array, to facilitate the matrix-based mathematical operations.^[17]

After conversion, the extreme values (taken to be values in the height data greater than $\pm 6\sigma$, where σ is the standard deviation for all the heights in that matrix) were filtered from the data sets. This step was necessary because some of the statistical parameters used to interpret the surface data are highly sensitive to outlier data points. Filtering consisted of setting the magnitude of any extreme value equal to the mean for that particular surface. Note that the number of affected data points for a given surface was typically fewer than 20 points (*i.e.*, <0.008 pct of the total number of data points). The residual matrix was used as the source for all subsequent assessments of the surface character. It was essential for these images to be well separated, to ensure that the surface data contained in each image was statistically independent (*i.e.*, no overlapping image data) and that the data properly represented the full range of surface characteristics.

III. RESULTS

A. Analysis of Topographic Data

The evolution of surface deformation is presented in Figure 1 as a function of the strain mode and strain level. The scanning laser confocal micrographs shown in this figure reveal the complexity of the surface features that are produced by the deformation process in a polycrystalline alloy. When viewed along the columns, the representative micrographs in this figure exhibit the evolution of surface deformation (*i.e.*, at 5 pct nominal true strain, 10 pct nominal true strain, and at the “failure” strain) in the equibiaxial, uniaxial, and plane strain modes. The estimated true strain levels for the failure condition are 30, 19, and 18 pct for the equibiaxial, uniaxial, and plane strain conditions, respectively. When viewed across the rows, the micrographs reveal the influence of the strain mode on the evolved surface at each strain level. The RD and tensile axis for the uniaxial and plane strain conditions are also indicated in each figure. Note that the 6- μm diamond surface contains scratches and other small remnants from the polishing procedure that may not be consistent with the directions indicated.

Probability density functions (PDFs) were calculated for each set of raw height data by extracting the individual data points from the five matrices acquired at

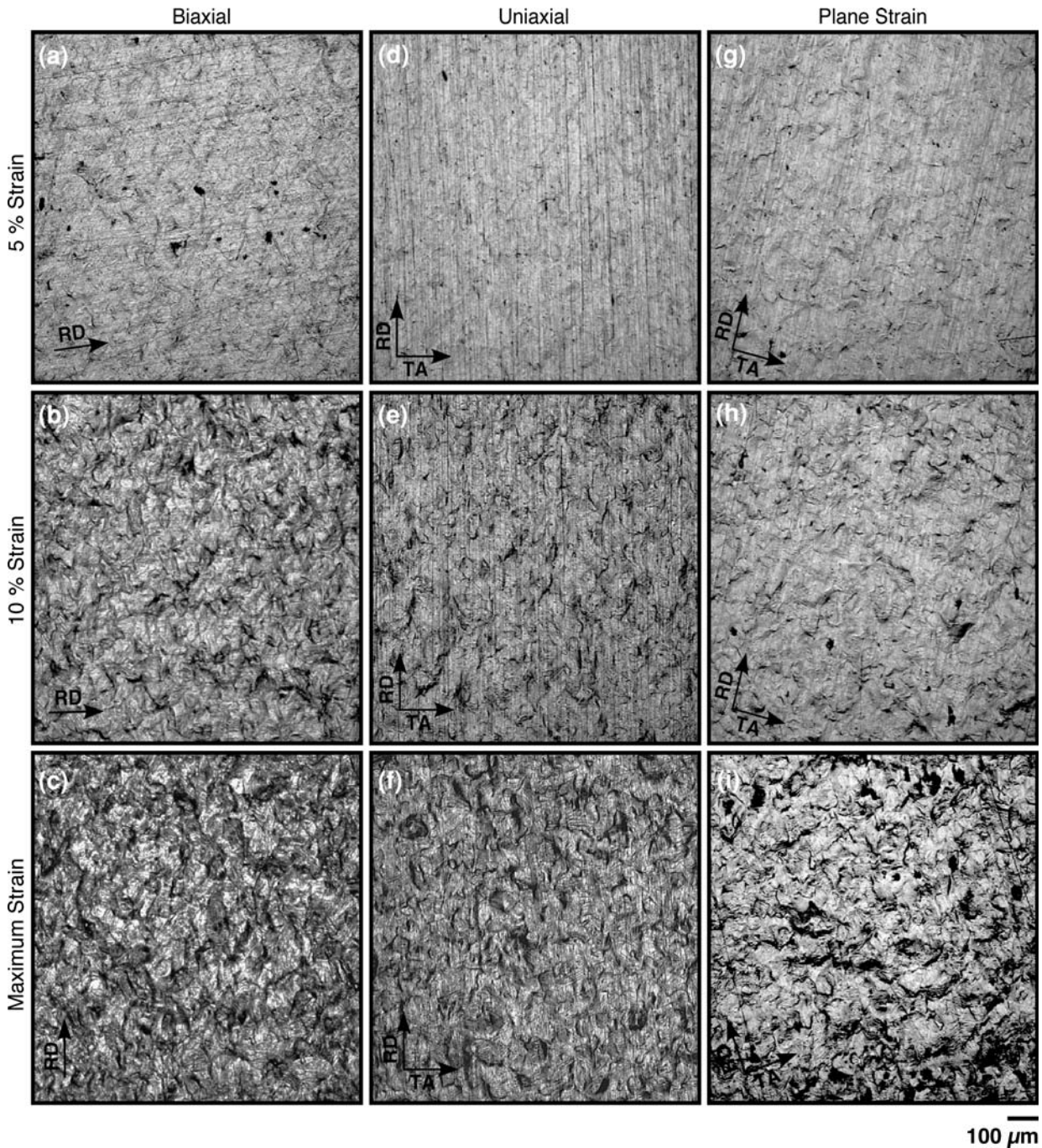


Fig. 1—Scanning laser confocal micrographs showing the surface structure of AA5754-O at three strain levels and in three strain modes. Images (a) through (c) are in equibiaxial strain; (d) through (f) are in uniaxial strain; and (g) through (i) are in plane strain. Images (a), (d), and (g) show the surfaces after 5 pct nominal true strain; (b), (e), and (h) show the surfaces after 10 pct nominal true strain; and (c), (f), and (i) show the surfaces at the maximum uniform strain.

each strain condition. An example of this construction is shown in Figure 2 for the data in the failure condition. The failure condition was selected for this plot because the variations among the individual data sets were generally larger at the higher strain levels. The envelopes in this figure are the upper and lower bounds of the PDF range for the five sets of surface height data acquired in each strain mode. As such, these envelopes reflect the magnitude of the variability in the raw surface height

data for each strain mode. Because the areas of each envelope are the same, the differences in the shapes of the envelopes also graphically illustrate the influence of the strain mode on the dispersion of heights about the mean (Sq).

The results of an analysis of the surface height data are shown in Table I. Note that this table contains both the true strain and the effective strain values. While the results of these analyses are expressed in terms of a true

strain level as a function of the strain mode, to facilitate a direct comparison of the influence of the strain mode on localization, a comparison of the localization behavior in terms of a normalized (*i.e.*, von Mises) uniaxial strain^[31] can be achieved with the effective strain values. Note that analyses based on these two strains will not necessarily produce identical results. As shown in References 17 and 32, the standard deviation σ and higher statistical moments can be determined directly for any matrix. Because the topographical matrices were leveled, the mean for each matrix is zero. The Sq values are consistent with other observations,^[13,33] in that they exhibit a proportional response to an increase in the plastic strain. While this proportionality is present in

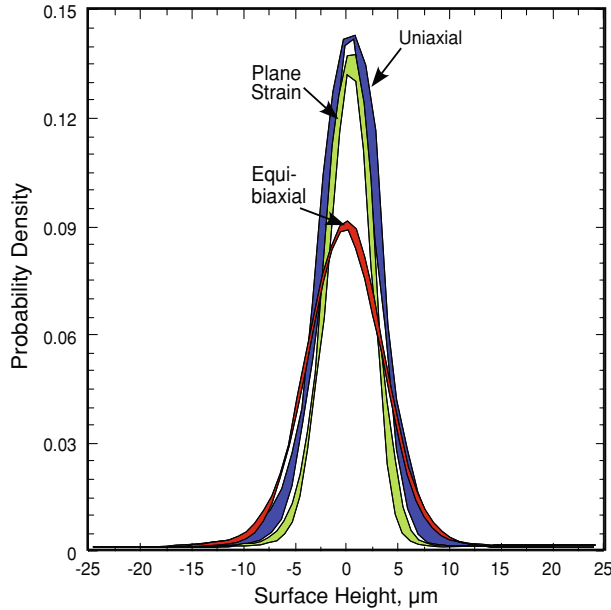


Fig. 2—Range of probability density distributions constructed from maximum and minimum raw height data values contained in the five topographies acquired at maximum uniform strain in each strain mode.

each strain mode, the Sq magnitude appears to reach a saturation value in the equibiaxial and plane strain conditions.

The surface skew Ssk (or third moment, σ_3) is a measure of the overall symmetry of the distribution of the raw height data about the mean plane; because it is normalized by the standard deviation, it is a dimensionless quantity. For a Gaussian distribution, $Ssk = 0$ and, as shown in Table I, the skew values are all slightly negative, indicating that a valley is somewhat more probable than a peak. Unlike the Sq values, the skews do not appear to reflect any systematic change with strain level or strain mode. The surface kurtosis Sku (or fourth moment, σ_4) is a measure of the overall shape of the height distribution about the mean plane and, like the skew, it is also normalized by the standard deviation and is dimensionless. For a Gaussian distribution, $Sku = 3$, and the Sku values shown in Table I are all somewhat greater than 3. This indicates that the raw height distributions have slightly sharper central peaks and longer tails than would occur if the distribution were Gaussian. As was the case with the skew values, no systematic change with strain is apparent in the kurtosis data.

B. Analysis of Localization Data

Analyses of all of the values contained within each set of raw height data provide details about the evolved surfaces with respect to the strain mode. They also reveal generalities about the relative trends resulting from the plastic deformation specific to a particular strain mode. However, these data cannot quantify the magnitude of a specific feature within the data. Quantification of the relationship between the surface roughness and strain localization requires an analysis that is based on a measure that describes the relative changes in the local surface heights. Data of this type can be obtained *via* a roughness parameter that is sensitive to the changes in the peaks and valleys on the surface. One such parameter is the maximum height of a profile Rt ,

Table I. Analysis of Raw Surface Height Data

Strain Path	True Strain	Effective Strain	Mean (μm)	Uncertainty* (μm)	Sq (μm)	Uncertainty (μm)	Skew [†]	Uncertainty	Kurtosis	Uncertainty
As polished	0.00	0.00	-8.26×10^{-9}	1.38×10^{-8}	0.921	0.027	-0.234	0.021	3.468	0.155
Equibiaxial	0.05	0.10	1.79×10^{-8}	2.00×10^{-8}	1.308	0.055	-0.338	0.075	4.004	0.194
	0.10	0.21	1.95×10^{-8}	3.84×10^{-8}	2.136	0.102	-0.465	0.055	4.149	0.163
	0.15	0.28	-1.23×10^{-8}	7.98×10^{-8}	2.606	0.078	-0.305	0.043	4.203	0.149
	0.20	0.41	-5.11×10^{-8}	3.90×10^{-8}	3.611	0.039	-0.291	0.058	4.164	0.131
	0.30	0.62	-1.19×10^{-7}	1.04×10^{-7}	3.886	0.180	-0.060	0.121	3.720	0.165
Uniaxial (RD \perp)	0.05	0.05	1.21×10^{-9}	2.04×10^{-8}	0.927	0.039	-0.375	0.022	3.783	0.114
	0.10	0.12	3.74×10^{-9}	5.89×10^{-8}	1.619	0.101	-0.563	0.101	4.289	0.266
	0.15	0.17	-8.62×10^{-9}	6.27×10^{-8}	2.320	0.117	-0.673	0.040	4.794	0.152
	0.19	0.20	3.51×10^{-8}	6.85×10^{-8}	3.137	0.647	-0.385	0.105	4.560	0.341
Plane strain (RD \perp)	0.05	0.07	1.22×10^{-8}	2.15×10^{-8}	0.952	0.052	-0.298	0.054	3.737	0.347
	0.10	0.11	4.50×10^{-8}	3.70×10^{-8}	1.455	0.053	-0.509	0.064	4.298	0.127
	0.15	0.17	2.67×10^{-8}	6.27×10^{-8}	2.510	0.520	-0.456	0.134	4.258	0.666
	0.18	0.19	1.17×10^{-8}	5.28×10^{-8}	2.304	0.272	-0.330	0.101	4.409	0.281

*Refers to the statistical uncertainty.

[†]The skew and kurtosis for a Gaussian distribution are normalized by the standard deviation and are dimensionless.

which is defined as the vertical distance between the highest and lowest points of a profile within a particular evaluation length.^[14] That is:

$$Rt = Rp + Rv \quad [1]$$

where Rp is the distance between the highest point of the profile and the mean line and Rv is the distance between the lowest point of the profile and the mean line within a particular evaluation length. (Note that heights lower than the mean plane are traditionally considered negative.) The Rt parameter is ideal for characterizing the surface conditions that promote critical strain localization and for quantifying the magnitudes of those surface conditions for several reasons. (1) This parameter is highly sensitive to a local change in the surface height and it is acquired through a straightforward calculation. (2) The length of the profile over which Rt is determined can range from a few data points within a profile to the entire profile, so the Rt parameter can track the changes in the surface height on a local or overall basis. (3) The magnitudes of the local surface extremes will change with strain to the point at which they reach a value that correlates with the onset of critical strain localization. (4) The Rt parameter can be easily determined for any two points within a particular region during a numerical simulation, thereby making changes in the local surface conditions directly integrable into formability models.

The statistical uncertainty associated with profile-based analysis can be minimized by extending the Rt parameter to a matrix form.^[17] This is accomplished by creating a Euclidean distance matrix.^[35] The construction of this matrix required subdividing a 512-row \times 512-column source matrix into smaller matrices consisting of 64 element cells (8 pixels/row \times 8 pixels/column). This created a differential matrix consisting of 4096 elements (*i.e.*, 64 \times 64 cells). The maximum difference in the surface height for a given cell, $Rt_{(i,j)}$, was determined from the 64 values contained within that cell. For this reason, $Rt_{(i,j)}$ is the maximum displacement normal to the mean plane in the source matrix at the coordinates of that cell. Because the matrix format preserves all of the spatial coordinates for an Rt cell by construction, both the magnitude and the location of each $Rt_{(i,j)}$ value are quantified by this method. Consequently, this technique links any feature in the source image to the corresponding change in magnitude of the local surface height and the level of resolution can easily be adjusted by altering the cell dimensions. Given that the mean grain size of this alloy is 40 μm , the 12.5 \times 12.5- μm cell used in this assessment was an acceptable level of resolution.

The results of the Rt matrix constructions are shown in Figure 3. The data used to construct the maps in Figure 3 are identical to those presented as images in Figure 1. The main distinction between Figures 3 and 1 is the change in resolution resulting from the Rt cell construction. The range of Rt magnitudes was mapped into a standard 8-bit color scale in which blue is low and red is high, so that the color of an individual cell directly reflects the local magnitude of Rt . The maps shown in Figure 3 exhibit the variations in Rt intensity produced

by the different strain conditions in exactly the same manner as in Figure 1. That is, when viewed across the rows, the maps reveal the local Rt intensity as a function of the strain mode at three different strain levels and, when viewed down the columns, the maps reveal the changes in the local Rt intensity as a function of the strain level for the three strain modes. While it differs with the strain mode, the number of high-intensity Rt cells increases progressively with the strain level, with the highest number of these cells occurring in the failure condition. Note that the scales for the Rt maps are different for each strain path and the significance of this difference will be addressed later in this article.

Upper- and lower-bound probability density envelopes were constructed for the Rt data in the same manner as was used for the height data (Figure 2). Again, the data for the failure condition are shown. There are two distinct differences between the PDF envelopes shown in Figures 4 and 2. First, the overall widths of the PDF envelopes are substantially greater for the Rt data than for the height data. This indicates a higher variability within the individual Rt data. Second, and more important, the overall shapes of the distributions are markedly different. The PDF envelopes shown in Figure 4 all exhibit a comparatively shorter left-hand tail and a substantially longer right-hand tail than those shown in Figure 2, which denotes that any analysis of the Rt data that is based on Gaussian statistics would not produce meaningful results.

C. Weibull Analysis

The general form in Figure 4 is consistent with that of an extreme value distribution (*i.e.*, the limiting distribution for a maximum or minimum of a large collection of random observations from the same distribution).^[36] Clearly, these data can be analyzed with several distributions,^[37] but the Weibull distribution is one of the more well known^[38,39] and was selected for this reason. Weibull statistics are used extensively in reliability predictions to estimate failure, because such predictions are concentrated on the incidence of statistically rare events (*i.e.*, the tail region). The Weibull distribution can be used to describe a unimodal distribution that has one disproportionately long tail, such as those shown in Figure 4.^[40-42]

A Weibull distribution has two forms: a two-parameter and a three-parameter distribution. Most Weibull analyses are based on a two-parameter distribution, because the third parameter, a “guaranteed,” or threshold, value (*i.e.* a value after which no events occur) is typically not known *a priori*. The Weibull distribution is continuous and has a probability density function of the form:^[42]

$$f_{\text{PDF}}(x; \alpha, \beta) = \left[\frac{\beta}{\alpha} \left(\frac{x}{\alpha} \right)^{\beta-1} \right] e^{-\left(\frac{x}{\alpha}\right)^\beta} \quad [2]$$

In this equation, ($x \geq 0$) and ($f_{\text{PDF}}(x; \alpha, \beta) = 0$ for $x < 0$). The two parameters, α , a scale parameter, and β , a shape parameter, must be real and >0 . Because of the extensive use in reliability prediction, the Weibull

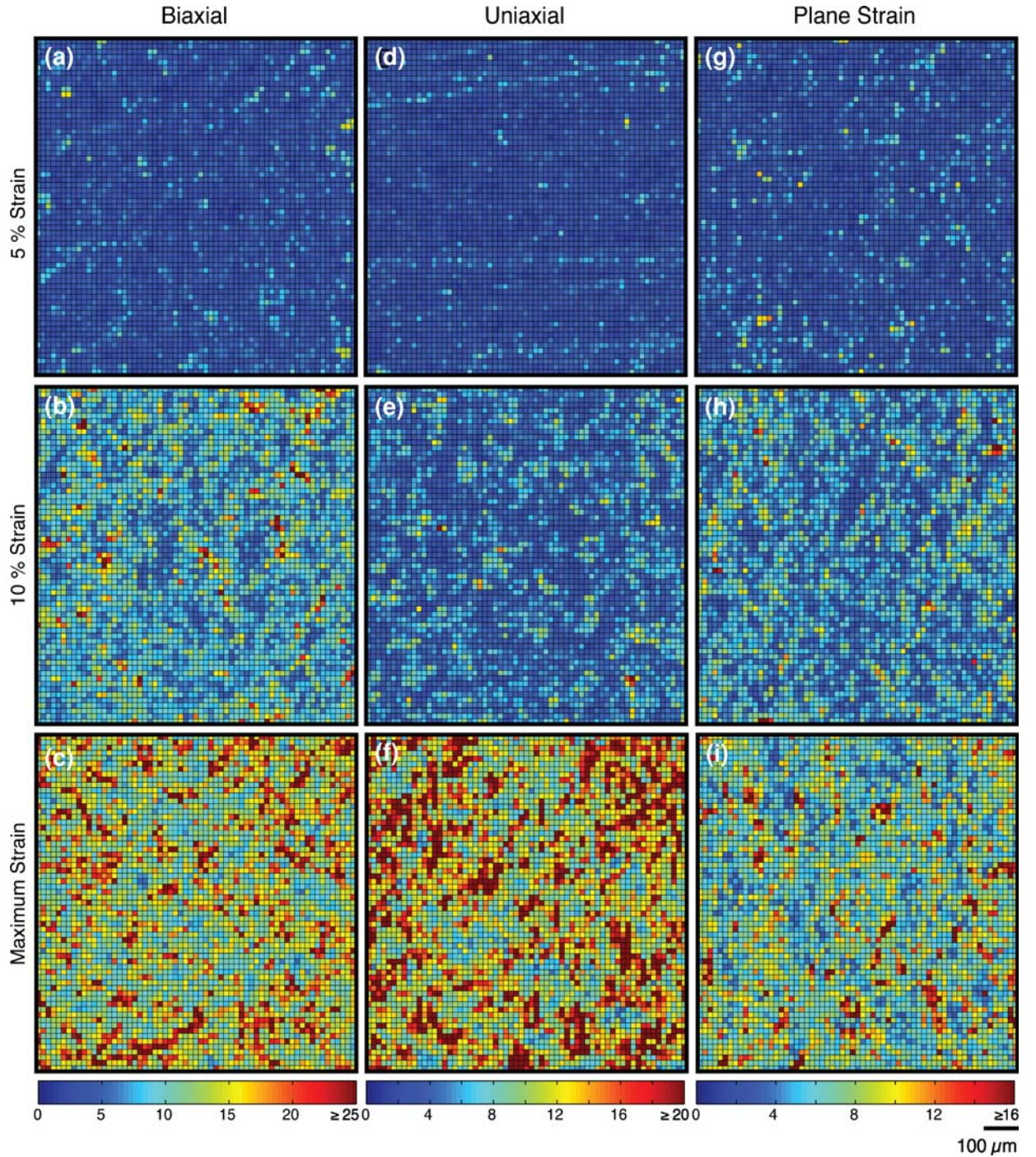


Fig. 3—Set of plots exhibiting the propensity for strain localization as a function of strain level and strain mode. Each plot is the Rt roughness data calculated for corresponding image shown in Fig. 1.

distribution is more commonly expressed in terms of the cumulative distribution function (CDF):

$$f_{\text{CDF}}(x; \alpha, \beta) = 1 - e^{-\left(\frac{x}{\alpha}\right)^\beta} \quad [3]$$

Note that, for a given strain level, the CDF is the probability P of the occurrence of an Rt magnitude that is less than or equal to any given Rt (*i.e.*, $f_{\text{CDF}}(Rt_{\text{given}}) = P(Rt \leq Rt_{\text{given}})$). In addition, the CDF

is bounded by the following conditions: $f_{\text{CDF}}(0) = 0$, and $f_{\text{CDF}}(\infty) = 1$.

The five sets of Rt values acquired in each strain condition were fitted with a Weibull distribution, using commercially available statistical software,^[43] and the mean α and β parameters for a given strain condition were determined from each set of α and β values using regression analyses. The results of the Weibull analysis are shown in Table II. The α and β values are plotted as a

function of the strain level for the equibiaxial, uniaxial, and plane strain modes in Figures 5 and 6, respectively. Note that the uncertainties in the α and β parameters were typically smaller than the plot symbols in both figures. The considerably smaller range exhibited by the β values in Figure 6 suggests that the shape parameter may be insensitive to changes in the strain state.

A Weibull distribution that describes the overall surface character can be estimated for each strain level and strain mode by substituting the mean α and β parameters calculated for those strain conditions into Eq. [3]. Because each Rt matrix contained 4096 values, a random data set with the same number of values was extracted from the Weibull distribution function for each strain condition, to represent the overall surface behavior. The results illustrate the relationships that are

likely to occur between the strain level, strain mode, and Rt magnitude. The characteristics of these estimated Weibull surface distributions are shown as the cumulative probability of the Rt magnitude plots for the equibiaxial, uniaxial, and plane strain conditions in Figures 8, 9, and 10, respectively. All three figures demonstrate systematic changes in the estimated Rt distributions with increasing strain. In the case of the equibiaxial and plane strain conditions, the overall shape of the CDF exhibits no appreciable changes after reaching approximately 20 pct in equibiaxial strain and 15 pct in plane strain mode. While saturation behavior also represents the behavior at failure in the uniaxial strain mode, none is apparent (Figure 10). At 0 pct and 5 pct strain, both the uniaxial and plane strain conditions do not appear to produce significant changes in the

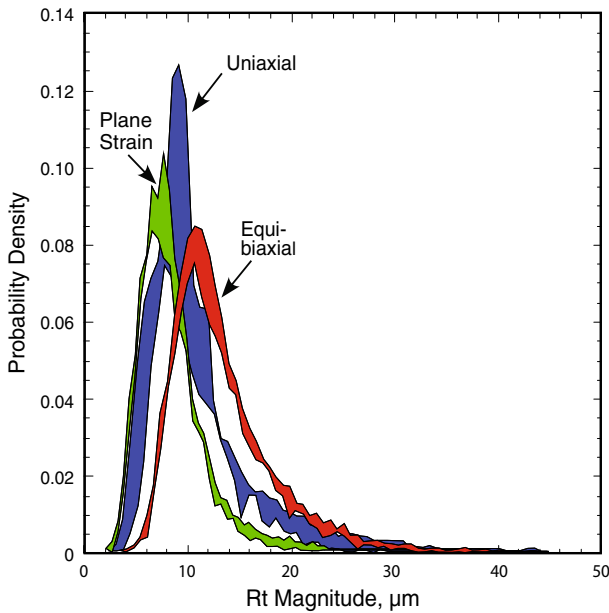


Fig. 4—Range of probability density distributions constructed from maximum and minimum Rt data contained in the five topographies acquired at maximum uniform strain in each strain mode.

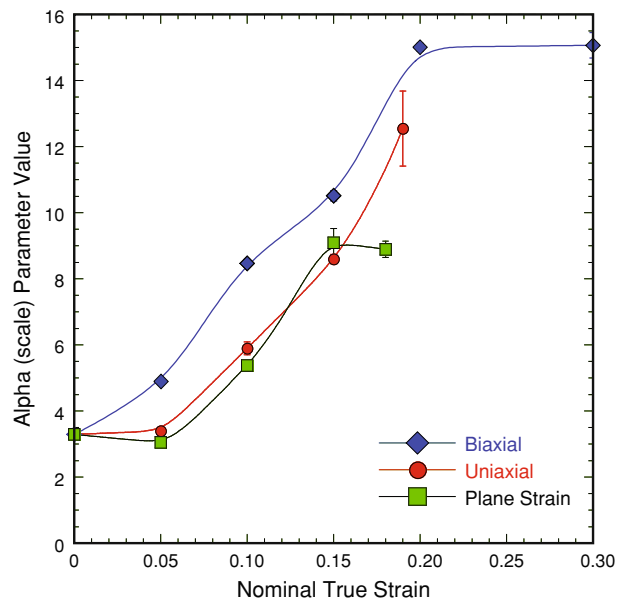


Fig. 5—Weibull scale (α) shown as a function of nominal true strain.

Table II. Analysis of Weibull Fit to Strain Localization (Rt) Data

Strain Path	True Strain	Mean	Variance	Skew*	Mode	Coefficient of Variation
As polished Equibiaxial	0	2.944	1.137	0.165	2.883	0.362
	0.05	4.338	3.100	0.294	4.083	0.406
	0.10	7.537	8.761	0.255	7.188	0.393
	0.15	9.349	14.055	0.280	8.844	0.401
	0.20	13.349	28.121	0.269	12.674	0.397
Uniaxial (RD ∞)	0.30	13.446	24.674	0.186	13.090	0.369
	0.05	3.0264	1.3408	0.2253	2.9132	0.383
	0.10	5.2469	4.3256	0.2662	4.9859	0.396
	0.15	7.6222	11.4687	0.4063	6.8647	0.444
Plane strain (RD ∞)	0.19	11.1392	22.1056	0.3416	10.3030	0.422
	0.05	2.7052	1.5291	0.4433	2.3957	0.457
	0.10	4.7749	4.1568	0.3559	4.3918	0.427
	0.15	8.0626	12.6252	0.3958	7.2942	0.441
	0.18	7.9014	10.7269	0.3195	7.3697	0.415

*The skew for a Weibull distribution is normalized by the standard deviation and is dimensionless.

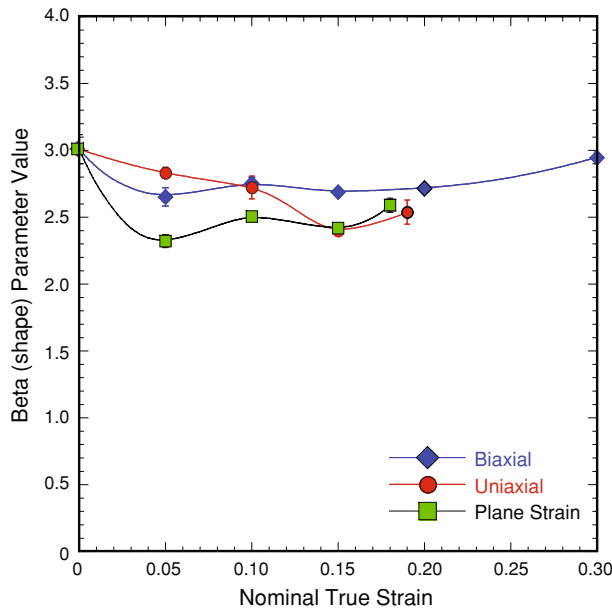


Fig. 6—Weibull shape parameters (β) shown as a function of nominal true strain.

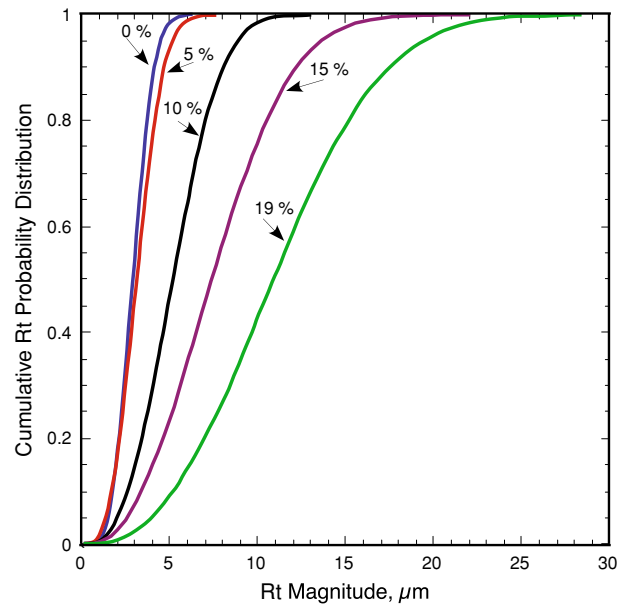


Fig. 8—Influence of uniaxial strain on the mean cumulative probability distribution of Rt . Each curve is the mean of the five Weibull scale and shape parameter values determined for that strain level, as shown in Figs. 5 and 6.

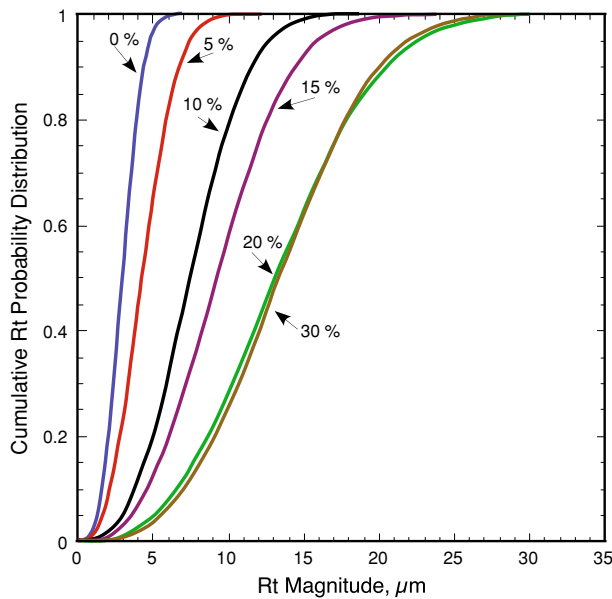


Fig. 7—Influence of equibiaxial strain on the mean cumulative probability distribution of Rt . Each curve is the mean of the five Weibull scale and shape parameter values determined for that strain level, as shown in Figs. 5 and 6.

shape of the Rt distribution, whereas significant changes are evident in the equibiaxial condition for the same strain levels.

The uncertainty present in the mean α and β values (Table II, Figures 5 and 6) produced a range of Rt probabilities for each strain condition shown in Figures 7, 8, and 9. As noted previously, the largest uncertainties were observed at the failure condition, for each strain mode. The degree of variation in the

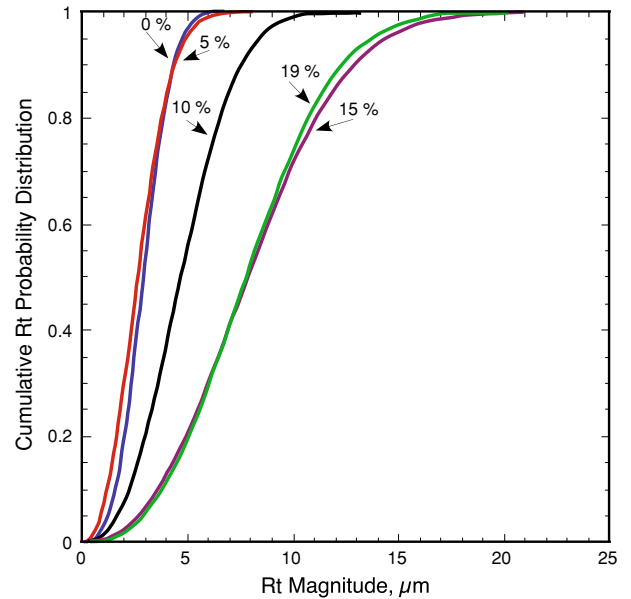


Fig. 9—Influence of plane strain on the mean cumulative probability distribution of Rt . Each curve is the mean of the five Weibull scale and shape parameter values determined for that strain level, as shown in Figs. 5 and 6.

estimated Rt distributions at failure is exhibited in the width of the uncertainty envelope associated with each strain mode in Figure 10. Unlike those shown in Figures 2 and 4, the envelopes in this figure are estimates of the largest uncertainties possible for the two Weibull parameters, as calculated from the α_{\min} , α_{\max} , β_{\min} , and β_{\max} in each strain mode. Note that the three envelopes in this figure do not exhibit significant changes in overall shape; this is consistent with the small

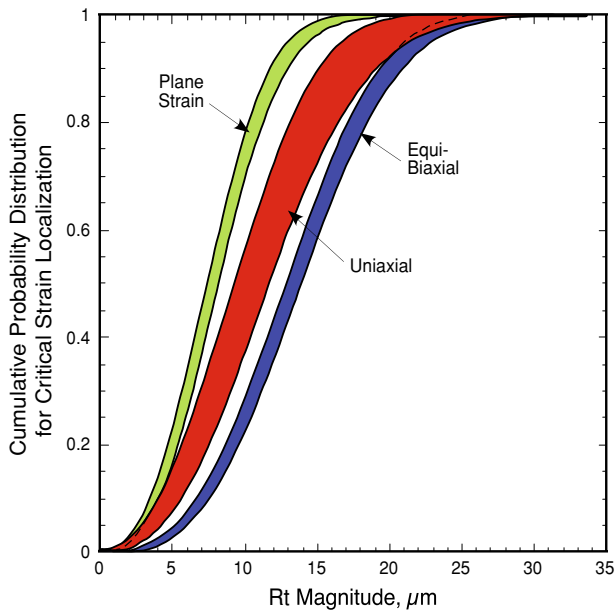


Fig. 10—Influence of strain mode on the cumulative probability distribution for critical strain localization. Each band is the maximum uncertainty envelope determined from the five Weibull scale and shape parameter values calculated at the maximum uniform strain in each strain mode.

variations observed in the shape parameter β . For this reason, variations in the scale parameter α have the greatest influence on the probability distribution. Given that the CDFs shown in Figure 10 are the probable Rt values predicted by the estimated Weibull surface distributions at failure, each envelope in this figure reflects the probability that a critical strain localization event will occur for this alloy in that strain mode. For example, an Rt value with a magnitude of $15 \mu\text{m}$ signifies that the probability for critical strain localization lies between approximately 60 and 68 pct in equibiaxial strain, 72 and 90 pct in uniaxial strain, and 96 and 99 pct in plane strain. Similarly, a 90 pct probability for critical strain localization corresponds to an approximate Rt value range between 11 and $12.5 \mu\text{m}$ for equibiaxial strain, 15 and $19 \mu\text{m}$ for uniaxial strain, and 19.5 and $21 \mu\text{m}$ in plane strain. The probability distribution envelopes in Figure 10 are, therefore, the basis for the color maps used in Figure 3. That is, the maximum of the color range (*i.e.*, the dark red) in Figure 3 corresponds to the magnitude of Rt on the CDF (rounded to the nearest whole number) at which the lower bound of the probability envelope reached a value of 95 pct for each strain mode, that is, the minimum Rt value at which the probability of the occurrence of a critical strain localization event is approximately 95 pct. Similarly, the color of each cell in Figure 3 directly corresponds to the local probability for critical strain localization.

IV. DISCUSSION OF RESULTS

The results of this study demonstrate that rigorous, matrix-based statistical analysis methods and appropriate

surface roughness parameters can be combined to create an effective technique for characterizing the surface inhomogeneities generated by plastic deformation. All of the topographic data acquired for this evaluation had a measurement resolution sufficient to assess the morphological conditions that promote strain localization developed by the three strain modes shown in Figure 1. These high-resolution data were used to map those morphological changes in two ways: one based on the raw height data and one based on the magnitude of the local extremes within the height data, with the primary intent being to determine whether carefully designed surface topography measurements can be used to reliably predict critical strain localization. The matrix methods used throughout are designed to handle large data sets efficiently. This enabled each surface condition to be based on five statistically independent topographic images (each consisting of 262,144 samples), as opposed to most traditional surface analyses, which are based on the average of a few linear profiles. This approach effectively maximized the statistical reliability of each surface characterization, resulting in extremely accurate analyses of the surface data and, because of this extraordinarily high number of samples, any differences between the individual data sets were directly attributed to variations in the surface character resulting from the local strain conditions, and not to measurement error.

The raw topographical maps reveal the relative influences of strain level and strain mode on the overall composition of the surface morphology. Thorough examination of the metallurgical history of the AA5754-O alloy revealed that, while this alloy exhibits PLC banding and some of the surface structure is likely due to inhomogeneities resulting from this PLC behavior, the morphologies shown in Figure 1 were primarily generated by dissimilarities in the deformation at the grain level. Because the deformed surfaces are highly sensitive to strain level and strain mode, the numerical results from the topographical analysis (Table I) reflect the variability in the local strain conditions produced by the strain level and strain mode. At low levels of plastic strain, the amount of deformation that occurs within each grain depends on the individual orientation,^[44,45] the local Taylor factor,^[46] and the constraints imposed by neighboring grains located at or just below the surface.^[47] That is, in those grains in which the orientation favors slip, the deformation occurs by primary slip in the interior regions. Conversely, in grains in which the slip conditions are not as favorable, the deformation tends to localize in the grain boundary regions because of the additional shear displacements required to produce grain rotation and maintain grain-to-grain contiguity.^[48] Recalling that the surface topography contains information about each active deformation mechanism, the composition of the surface roughness must change accordingly with strain at the grain level such that neighboring surface grains with the same level of macroscopic strain can exhibit appreciably different surface roughnesses. The higher dislocation densities produced by localized work hardening makes deformation by primary slip increasingly more difficult,

with additional plastic strain resulting in the activation of additional deformation mechanisms. Furthermore, plastic deformation is a volume-conserving process, and each strain mode in this evaluation imposes different degrees of freedom and effective levels of strain for the deformation of the sheet.^[31] Therefore, the local conditions required to activate a particular deformation mechanism must differ with the strain mode, thereby directly influencing the composition of the measurable surface roughness. For this reason, the micrographs shown in Figure 1 also exhibit the manner in which the physical constraints imposed by the strain modes exacerbate the local differences in the plastic flow.

Considering that Rt is effectively the scalar projection of the height gradient, the strain localization maps in Figure 3 reflect the magnitude of the changes in the local peak-to-valley height for the surfaces shown in Figure 1. Furthermore, because it is based on a group and not on individual pixels, an individual Rt cell is a coarse-grained measure of the differential topography on a local level. In contrast to the maps based on the raw surface data, the Rt maps provide a basis for quantifying the magnitude of the microstructural dissimilarities that promote critical strain localization (*e.g.*, cracks, splits and tears, and necking).

These maps also tend to visually accentuate more macroscopic surface features in the data, especially at the failure condition in the uniaxial strain mode (Figure 3(f)), in which PLC banding may have had the strongest effect on the surface character.^[49] A discussion of the intricacies of PLC banding lies outside this investigation; however, the aspect of this behavior that is germane to this particular study is the evolution of the macroscopically scaled planar bands that emerge in a periodic fashion on the specimen surface.^[50,51] Even though recent research by Halim *et al.*^[52] suggests that failure and PLC band formation may be independent, it is generally believed that PLC banding enhances strain localization by focusing deformation into the regions surrounding the PLC bands.^[53]

The different widths of the uncertainty envelopes associated with the estimated Rt distributions in Figure 10 suggest that PLC banding may also have had an influence on the variability of the predicted Rt behavior by increasing the variability in the Weibull scale parameter α . In this figure, the envelopes associated with the equibiaxial and plane strain conditions are considerably smaller with respect to the uniaxial condition, which also exhibited the greatest range in α . This is consistent with the literature that describes the relationship between PLC banding and strain mode.^[54]

Numerous cells in Figure 3 exceeded the Rt magnitude predicted by the Weibull analysis to produce critical localization in Figure 10, but failure did not occur. This behavior implies that the simple occurrence of an individual cell with a critical Rt magnitude is insufficient for initiating critical strain localization. That is, failure may involve a threshold event or possibly a nucleation and growth process involving several cells that exceed the critical Rt magnitude. Further examination of Figure 3 revealed that, as the strain level increases, groups of cells with similar relative probabilities

for strain localization (*i.e.*, structure), do appear to form within the Rt maps. Clearly, this structure is associated with the color scale used for this analysis; the existence of this structure, however, cannot be assumed an artifact *a priori*. An assessment of the influence of the Rt structure on strain localization requires detailed analyses of the spatial arrangements that may exist within the Rt data. Research is in progress to determine whether structure is, indeed, present in the Rt data and whether or not it has any influence on strain localization.

V. CONCLUSIONS

Rigorous three-dimensional matrix-based statistical analysis methods were developed and integrated with high-resolution topographical imaging to assess critical details related to the way in which changes in microstructure influenced the evolution of plastic deformation and strain localization in a commercial AA5754-O aluminum alloy sheet in three in-plane strain modes. The analysis of the surface data involved mapping the topographic data in two distinctly different but complementary forms. The first examined the characteristics that were present in the raw surface data at different strain levels in the three strain modes. The results revealed that the general composition of the surface roughness was sensitive to the strain level and strain mode. However, the evaluation of the raw surface data did not reveal any substantive information about the propensity for strain localization in any strain condition. The second extended a profile-based surface roughness parameter (Rt) to a matrix form, thus enabling a three-dimensional quantification of the microstructural conditions that promote strain localization. This calculation filtered the raw surface data and accentuated more macroscopic features in the topographies. In addition to revealing that the conditions for strain localization were sensitive to the strain mode, the results indicated that the Rt data could be well characterized with a two-parameter Weibull distribution.

The results from both analyses show that both the raw and the filtered surface data exhibited dissimilarities in the deformation at the grain level that were produced by the individual strain modes. The influence of the strain path was reflected in the widths of the envelopes associated with the raw height distributions, the Rt distributions, and the uncertainties associated with Weibull predictions of the probabilities for the onset of strain localization in the three strain modes. Furthermore, the widths of the uncertainty envelopes associated with the Rt distributions and the Weibull predictions reflect a dependence on the strain mode that suggests that PLC banding might have had an influence on the Rt data.

The results of this evaluation clearly demonstrate that the topographical conditions that promote critical strain localization can be assessed directly from rigorous analyses of accurate surface roughness data and that an accurate and straightforward probabilistic expression capturing the subtleties produced by these microstructural

conditions can be developed from such an assessment. These results also suggest that the propensity for strain localization is a stochastic process that can be reliably predicted with Weibull statistics. Numerous Rt cells that exceeded the predicted critical Rt magnitude were “observed” in the Rt maps at strains at which failure did not occur. This implies that failure could involve a nucleation and growth process requiring several Rt cells that exceed the critical magnitude. As noted throughout this article, local variations in surface structure are known to have a profound influence on the reliability of the primarily deterministic numerical models used to predict the onset of localization. Therefore, the incorporation of a simple expression that reliably estimates the probability of critical strain localization (such as the one developed in this study) could greatly enhance the accuracy of these numerical models.

REFERENCES

1. T. Foecke, M.A. Iadicola, A. Lin, and S.W. Banovic: *Metall. Mater. Trans. A*, 2007, vol. 38A, pp. 306–13.
2. T. Pardoen and Y. Brechet: *Philos. Mag.*, 2004, vol. 84, pp. 269–97.
3. Z. Marciniak and K. Kuczynski: *Int. J. Mech. Sci.*, 1967, vol. 9, pp. 609–20.
4. J.E. Bird and J.L. Duncan: *Metall. Trans. A*, 1981, vol. 12A, pp. 235–41.
5. F. Barlat, R.C. Becker, Y. Hayashida, Y. Maeda, M. Yanagawa, K. Chung, J.C. Brem, D.J. Lege, K. Matsui, S.J. Murtha, and S. Hattori: *Int. J. Plast.*, 1997, vol. 13, pp. 385–401.
6. A.J. Beaudoin, A. Acharya, S.R. Chen, D.A. Korzekwa, and M.G. Stout: *Acta Mater.*, 2000, vol. 48, pp. 3409–23.
7. D. Rabbe, M. Sachtleber, H. Weiland, G. Scheele, and Z. Zhao: *Acta Mater.*, 2003, vol. 51, pp. 1539–60.
8. R. Becker and O. Richmond: *Modell. Simul. Mater. Sci. Eng.*, 1994, vol. 2, pp. 439–54.
9. H.A. Al-Quershi, A.N. Klein, and M.C. Fredel: *J. Mater. Proc. Technol.*, 2005, vol. 170, pp. 204–10.
10. J. Savoie, M. Jain, A.R. Carr, P.D. Wu, K.W. Neale, Y. Zhou, and J.J. Jonas: *Mater. Sci. Eng., A*, 1998, vol. 257A, pp. 128–33.
11. P.D. Wu, D.J. Lloyd, M. Jain, K.W. Neale, and Y. Huang: *Int. J. Plast.*, 2007, vol. 23, pp. 1084–1104.
12. W.B. Liewers, A.K. Pilkey, and D.J. Lloyd: *Acta Mater.*, 2004, vol. 52, pp. 3001–07.
13. M.R. Stoudt and J.B. Hubbard: *Acta Mater.*, 2005, vol. 53, pp. 4293–4304.
14. R. Becker: *Acta Mater.*, 1998, vol. 46, pp. 1385–1401.
15. Z. Zhao, R. Radovitzky, and A. Cuitino: *Acta Mater.*, 2004, vol. 52, pp. 5791–5804.
16. K. Osakada and M. Oyane: *Bull. JSME*, 1971, vol. 14, pp. 171–77.
17. M.R. Stoudt, J.B. Hubbard, and S.A. Janet: *Mater. Sci. Technol.*, 2008, vol. 24, pp. 253–60.
18. M. Cai, M.R. Stoudt, L.E. Levine, and J.T. Dickinson: *Philos. Mag.*, 2007, vol. 87, pp. 907–24.
19. H.J. Frost and M.F. Ashby: *Deformation-Mechanism Maps: The Plasticity and Creep of Metals and Ceramics*, Pergamon Press, Oxford, United Kingdom, 1982.
20. G.W. Greenwood: *Mater. Sci. Eng., A*, 2005, vols. 410–411, pp. 12–15.
21. F.A. Mohamed and T.G. Langdon: *Metall. Trans.*, 1974, vol. 5, pp. 2339–45.
22. S.W. Banovic, M.A. Iadicola, and T. Foecke: *Metall. Mater. Trans. A*, 2008, vol. 39A, pp. 2246–58.
23. M.A. Iadicola, T. Foecke, and S.W. Banovic: *Int. J. Plast.*, 2008, vol. 24, pp. 2084–2101.
24. A.H. Cottrell: *Philos. Mag.*, 1953, vol. 44, pp. 829–32.
25. L.P. Kubin and Y. Estrin: *Acta Metall. Mater.*, 1990, vol. 38, pp. 697–708.
26. P.G. McCormick: *Acta Metall.*, 1971, vol. 19, pp. 463–71.
27. Anonymous: *Aluminum Standards and Data 2003*, The Aluminum Association, Washington, DC, 2003.
28. G.F. VanderVoort: *Metallography Principles and Practice*, ASM INTERNATIONAL, Materials Park, OH, 1999.
29. Anonymous: *1993 Annual Book of ASTM Standards, Section 3, Metals Test Methods and Analytical Procedures*, ASTM, Philadelphia, PA, 1993.
30. K.S. Raghavan: *Metall. Mater. Trans. A*, 1995, vol. 26A, pp. 2075–84.
31. G.E. Dieter: *Mechanical Metallurgy*, McGraw-Hill, New York, NY, 1986.
32. J.B. Hubbard, M.R. Stoudt, and L.E. Levine: *J. Appl. Phys.*, 2007, vol. 102, pp. 1–10.
33. M.R. Stoudt, J.B. Hubbard, S.P. Mates, and D.E. Green: *SAE Trans. J. Mater. Manuf.*, 2006, vols. 114–115, pp. 183–90.
34. Anonymous: *ASME Designation B46.1-2002: Surface Texture (Surface Roughness, Waviness and Lay)*, ASME, New York, NY, 2002.
35. J. Dattorro: *Convex Optimization & Euclidean Distance Geometry*, MeBoo Publishing, Palo Alto, CA, 2005, pp. 219–314.
36. S. Kotz: *Extreme Value Distributions: Theory and Applications*, Imperial College Press, London, 2002.
37. N. Balakrishnan and V.B. Nevzorov: *A Primer on Statistical Distributions*, J. Wiley & Sons, Hoboken, NJ, 2003.
38. J. Galambos, J. Lechner, and E. Simiu: *Extreme Value Theory and Applications*, Kluwer Academic Publishers, Dordrecht, The Netherlands, 1994.
39. W. Weibull: *J. Appl. Mech.*, 1951, vol. 18, pp. 293–97.
40. J.E. Shigley and C.R. Mischke: *Mechanical Engineering Design*, McGraw-Hill, New York, NY, 1989, pp. 165–71.
41. K.C. Kapur: *Reliability in Engineering Design*, Wiley, New York, NY, 1977.
42. Anonymous: *Weibull Distribution*, Wikipedia, The Free Encyclopedia, 2008.
43. MATLAB version 7.4 (R2007a), The MathWorks. Inc, Natick, MA, 2007.
44. E.J. Moore: Doctoral Dissertation, University of Maryland, Baltimore County, MD, 2006.
45. E.J. Moore, M.R. Stoudt, and R.C. Reno: *TMS Lett.*, 2005, vol. 2, pp. 135–36.
46. G.I. Taylor: *J. Inst. Met.*, 1938, vol. 62, pp. 307–24.
47. M.R. Stoudt and R.E. Ricker: *Metall. Mater. Trans. A*, 2002, vol. 33A, pp. 2883–89.
48. M.F. Ashby: *Philos. Mag.*, 1970, vol. 21, pp. 399–424.
49. J.D. Kang, D.S. Wilkinson, J.D. Embury, M. Jain, and A.J. Beaudoin: *Scripta Mater.*, 2005, vol. 53, pp. 499–503.
50. A. Inagaki, T. Komatsubara, and H. Inagaki: *Z. Metallkd.*, 1999, vol. 90, pp. 427–33.
51. P.J. Worthington and B.J. Brindley: *Philos. Mag.*, 1969, vol. 19, pp. 1175–78.
52. H. Halim, D.S. Wilkinson, and M. Niewczas: *Acta Mater.*, 2007, vol. 55, pp. 4151–60.
53. J.M. Robinson: *Int. Mater. Rev.*, 1994, vol. 39, pp. 217–27.
54. M. Li and D.J. Lege: *J. Eng. Mater. Technol.*, 1998, vol. 120, pp. 48–56.